Intrinsic dense twinning via release of native strain

Xianqi Song [a,1], Chang Liu [a,b,1], Quan Li [a,b,*], Yanming Ma [a,b,*], Changfeng Chen [c,**]

[a] State Key Lab of Superhard Materials and Key Laboratory of Material Simulation Methods & Software of Ministry of Education, College of Physics, Jilin University, Changchun 130012, China
[b] International Center of Future Science, Jilin University, Changchun 130012, China
[c] Department of Physics and Astronomy, University of Nevada, Las Vegas, Nevada 89154, USA

ARTICLE INFO

ABSTRACT

Icosahedral boron-rich solids exhibit outstanding mechanical properties, but the crystal structure of this prominent class of materials has long remained enigmatic. Here, we report on a surprising discovery of an unprecedented twinning induced structural stabilization that creates highly nanotwinned crystal structures that are stabler than the prevailing single crystal structure comprising complex multi-atom structural units. This phenomenon is showcased via a symmetry guided optimization process that produces a series of increasingly nanotwinned B_4C structures with progressively lower energy below that of the single crystal, and this behavior also occurs in multiple other boron-rich solids. These findings unveil a distinct paradigm of defect (twinning) induced structural stabilizing mechanism that reduces energy via release of native strains built in the complex structural units of the single crystal, creating an exceptional category of materials that comprise multiple domains of intrinsic dense twinning in the crystal structures.

1. Introduction

The light-element boron-rich compounds B_nX (X=C, N, etc.) possess low density and high strength that are favorable for wide applications [1–4]. The constituent atoms have similar electronegativity values that facilitate formation of B-X covalent bonds, and multi-center boron bonds promote diverse bonding patterns [5], generating structural units containing a large number of atoms, which greatly increases the difficulty for crystal structure determination. Close atomic radii of the X and B atoms make it hard for experimental distinction of atomic occupation sites, hindering accurate structural characterization. Early studies introduced the rhombohedral prototype structure containing icosahedral cages [6], which has been adopted for a large family of compounds, such as B_4C, $B_{13}C_2$, α-B, and B_6X (X=N, O, etc.) [7]. Later advances identified that the stable structure of B_4C comprises $B_{11}C_p$(CBC) icosahedral units with carbon atom substituting for boron on the polar site (C_p) instead of the equatorial site (C_e) of the B_{12} unit while the displaced boron atom joins the original three-atom carbon segment to form a CBC chain in the crystal structure [8–11]. Employing various crystal structure search methods [12–15], several recent studies predicted

nonrhombohedral structures of icosahedral boron-rich solids [16–19] e. g., τ-B_4C slightly less stable than R-B_4C [17] and τ-B_6O even more stable than R-B_6O [19].

Grain boundaries are a common type of structural defects, among which coherent twin boundaries (TBs) are most stable because the favorable lattice matching at the boundary minimizes the energy cost of forming the defective TBs relative to the single crystal [20]. Crystal twinning enriches structural diversity of boron-rich complex covalent bonding solids. Synthesized boron carbides often contain dense nanotwins with various symmetric and asymmetric polytypic microstructures [17,21–28], and first principles calculations show that twinning raises the system energy but may also strengthen the resulting crystal structure in B_4C and many other icosahedral boron-rich solids [19,29–33], similar to observations made in nanotwinned diamond and cubic boron nitride [34–37]. Despite extensive past studies, there is still a lack of understanding of the nature of TBs in boron-rich solids, especially the rich variety and complex hierarchy of their structural forms and the atomistic mechanisms that determine their relative stability.

Here, we report on an intriguing crystal twinning induced structural stabilization mechanism that optimizes the relation of local bonding
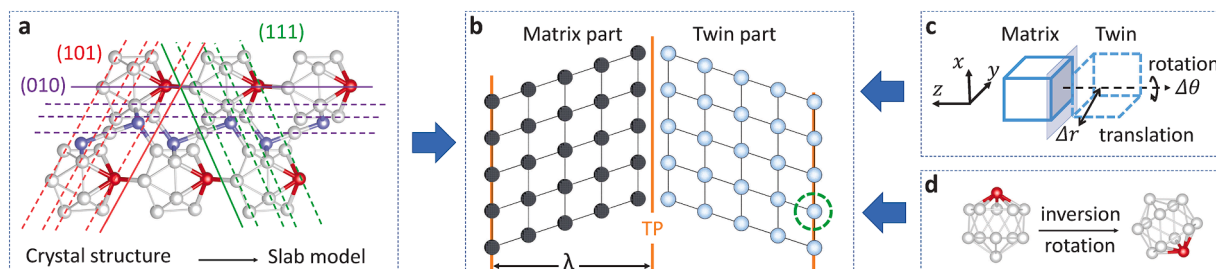

Fig. 1. (a) A slab is cut from the single crystal to construct the matrix part of a twinned structure of B$_4$C, where boron atoms, carbon atoms on CBC chains and carbon atoms on icosahedra are represented by gray, lavender, and red spheres, respectively. The solid lines indicate suitable cutting planes in the (101), (111), and (010) orientations for building the matrix part, while the parallel dotted lines show improper cutting planes. (b) The twinning structure by joining the matrix part and twin part at the twin plane. The spacing between adjacent TPs is set by the thickness (λ) of the slab. (c) Splicing the matrix and twin part via selective translation or rotation of the twin part. (d) Adjustment of local structure units (e.g., icosahedral B$_{11}$C cage) via selective inversion or rotation. (For interpretation of the references to colour in this figure legend, the reader is referred to the web version of this article.)

symmetry and global stacking symmetry in a broad class of icosahedral boron-rich solids, which host complex multi-atom cages and chains as the basic structural building units. Remarkably, a symmetry guided optimization procedure produces twinning structures with energies that are below that of the established single crystal and become progressively lower with rising defect (twinning) density. This behavior runs counter to the common wisdom that structural defects would raise the crystal energy. Such unusual behaviors stem from a twinning-mediated release of native strains inherent in the complex bonding network, and this phenomenon is widely present in a variety of icosahedral boron-rich solids that are conducive to hosting multiple energetically close densely nanotwinned crystal domains. We identified a broader variety of nanotwinned boron-rich crystals that exhibit energies only slightly above that of the single crystal. These findings showcase a robust twinning-induced crystal stabilization mechanism among a prominent class of complex covalent bonding crystals, creating a new paradigm that enriches fundamental structure-stability relations for defects in crystalline solids.

2. Computational methods

2.1. First-principles calculations

The first-principles total-energy calculations are carried out using local density approximation exchange correlation potential [38,39] as implemented in the Vienna *Ab initio* Simulation Package [40], adopting the projector augmented wave approach [41] to describe electron-ion interaction with $2s^2 2p^1$ and $2s^2 2p^2$ valence electron configurations for boron and carbon atoms, respectively. The plane wave basis set is constructed with an energy cutoff of 600 eV and the Brillouin zone is sampled under the Monkhorst-Pack scheme [42] with a k-point resolution of $2\pi \times 0.03$ Å^{-1}, achieving an energy convergence around 1 meV per atom. Phonon dispersion curves were calculated using finite displacements approach as implemented in the Phonopy code [43]. *Ab initio* molecular dynamic (AIMD) simulations are performed within a canonical ensemble (NVT) and a time step of 2 fs at 300 K adopting a 540-atom supercell (3×3×1 cells). The atomic mean-square displacement (MSD) is defined by MSD$(t) = (1/N) \sum_{i=0}^{N} \langle [r_i(t) - r_i(0)]^2 \rangle$, where N is the total number of atoms, $r_i(0)$ is the initial position of atom i, $r_i(t)$ is the atomic position at time t and $\langle \cdots \rangle$ means an ensemble average. Stress-strain relations are calculated using an established method [44–47] which imposes appropriate deformations on the unit cell manually to simulated various loading conditions, e.g., compression and shear, and the shape of the unit cell together with atomic relaxation is determined completely at each step by the constrained structural optimization to achieve the quasi-static deformation process with a strain increment of 0.01. Meanwhile, the other five stress-tensor components and the force on each atom become trace, typically less than 0.1 GPa and

0.01 eV/Å, respectively.

2.2. Construction of twinned B$_4$C crystal

The R-B$_4$C has been widely accepted as the single-crystal structure in the previous literatures, and thus taken as the starting single-crystal structure. A twinned B$_4$C crystal is constructed by cutting a slab from its single crystal along a selected crystal plane, which serves as the twin plane (TP), then placing the mirror image of the slab across the TP to form the twinned structure. There are, however, constraints imposed by symmetry and energy that guide the choice of the most proper TPs. For example, the (1$\bar{1}$0) plane is a mirror-symmetry plane of single-crystal B$_4$C and thus cannot serve as a TP since the construction simply reproduces the original single crystal. On the other hand, the (111) plane can serve as a TP, but relative displacements are needed to match the matrix and twin part, as illustrated in Fig. S1a. Here, the TPs are the vertical bisectors of the CBC chain with the B$_{11}$C cages located on both sides of the TPs. Further adjustments of carbon-atom positions are made to avoid the high-energy intra-cage C$_e$ atoms and inter-cage C$_p$-C$_p$ bonds. Meanwhile, the (101) plane that goes through the center B atom on the CBC chain does not bisect the atomic chain, making it an improper TP choice; but the (101) plane that separates adjacent icosahedra and CBC chains can serve as a proper TP, as illustrated in Fig. S1b, where the equatorial-position planes or polar-position planes are not parallel to the TP. The structural adjustments relative to the single crystal introduced to achieve adequate bonding at the TP renders these twinned crystals to become less energetically favorable than the single crystal. The lowest energy twined crystal is built with the TPs aligned in the (010) orientation as described in the main text of the paper. Here, the TPs traverse the B$_{11}$C cages and divide them into equal halves without altering the CBC chains or breaking and rearranging bonds across the TPs, resulting in the most energetically favorable twinned B$_4$C crystal structure.

3. Results and discussion

3.1. Principles and procedures in constructing twinned structure

We construct and evaluate TBs in a variety of boron-rich solids, focusing on the effect of bonding symmetry on the total energy. The procedure for constructing twinning structures is illustrated in Fig. 1 for the exemplary case of B$_4$C. The first step is to identify a suitable twin plane (TP) among various crystal orientations and cut a slab from the single crystal (Fig. 1a). A TB is then formed by joining a pair of matrix and twin parts that are in mutual mirror symmetry at a specific TP with adjustable slab thickness (Fig. 1b). Icosahedral boron-rich compounds contain complex, non-atom structural units, such as cages and chains, and different TP choices even with the same Miller index may lead to distinct TBs. To obtain optimal TP, it is imperative to find good bonding
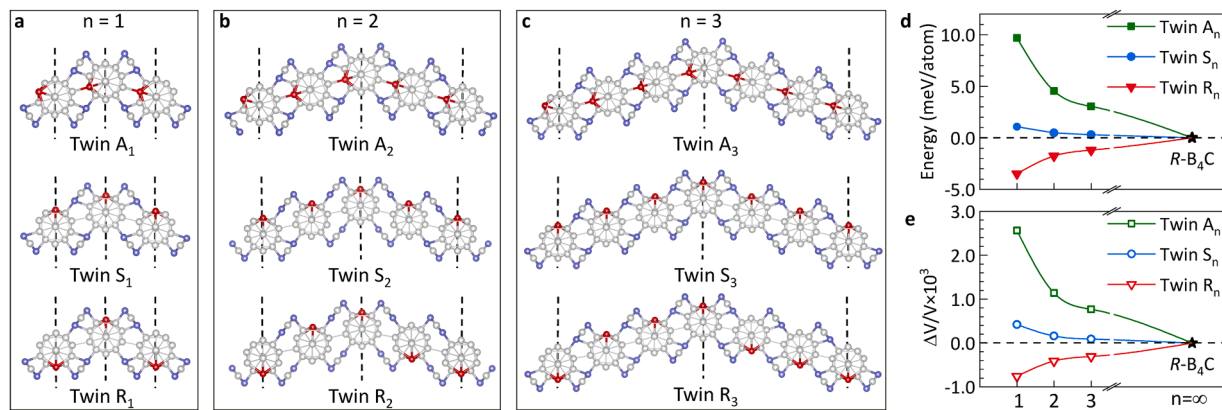
Fig. 2. Three lowest-energy twinned crystals, Twin A_n, Twin S_n, and Twin R_n (Tables S1-S3), with distinct (010) slab thicknesses marked by structure-unit index (a) n=1, (b) n=2, and (c) n=3. (d,e) Energy and volume changes relative to the single crystal values. All the twinned crystals tend to the prevailing single crystal rhombohedral R-B$_4$C ($n \to \infty$).

connections between the matrix and twin part via crystal matching operations, such as translational and rotational adjustments, as illustrated in Fig. 1c. Positional variations of the structural units with different bonding patterns (Fig. 1d) may also notably impact structural stability.[36] Since the TB dictated mirror symmetry alters the atomic positions and crystal orientations of the structural units from those of the single crystal, compatibility of the local structural-unit bonding symmetry with global TB stacking symmetry plays a crucial role in minimizing the twinning energy.

Following the procedure outlined above, we have constructed and examined a series of twinned B$_4$C crystals based on the prevailing single-crystal structure R-B$_{11}$C$_p$(CBC). We find that bonding alignment at TP has a major impact on the relative stability of the resulting twinning structure. The twinned crystals with (111) and (101) oriented TPs (Fig. S1) require substantial bonding adjustments across the TPs as outlined in Fig. 1c, d, including new bonding connections to avoid the energetically unfavorable intra-cage C$_e$ position and intercage C$_p$-C$_p$ bonds. For the (010) oriented TP, TBs can be formed via orientational adjustments of the CBC chains and icosahedral cages to satisfy the mirror symmetry without the need to change any bonding connections inherited from the original single crystal. This preservation of bonding connectivity makes the (010)-twinned B$_4$C energetically favorable.

3.2. Structural stability of twinned B$_4$C crystals

Twinned crystals possess the characteristic symmetry with the lattice sites on the two sides of TPs forming mutual mirror images; but for multi-component materials, occupation of the lattice sites by different atomic species can lead to bonding configurations that do not strictly obey the mirror symmetry. In the case of B$_4$C, a (010) oriented twin model, referred to as Twin A_n hereafter (Fig. 2a–c) was previously proposed. In this structure, the lattice sites obey the TP mirror symmetry before the structural relaxation caused by atomic (carbon) substitution in the otherwise all-boron B$_{12}$ icosahedral cage; however, the energetically dictated incorporation of the carbon atom generates distortion in the resulting B$_{11}$C cage and breaks the structural symmetry at the atomic bonding level [8–11]. The bonding pattern in the twinned crystal becomes asymmetric about the TP; consequently, the resulting Twin A_n crystals no longer obey the mirror symmetry, thus violating the basic requirement for TBs. To remedy this problem, we have constructed two different (010) oriented twinned crystals by rotating the B$_{11}$C cage to align the carbon atoms on the cages inside TPs to satisfy the full mirror symmetry of the structure units relative to the TP at the atomic bonding level. The resulting twinned crystals, referred to as Twin S_n and R_n, respectively, exhibit detailed matching between the local (on-cage) bonding and TP mirror symmetry. Twin S_n and R_1 possess full mirror

symmetry on the TP at the atomic level (including the mirror symmetry of every cage on the TP and the mirror symmetry between the cages over a long distance). The other C$_p$-C$_p$ type twins [Twin R_n (n>1), Twin A_n and gradient twins] or C$_p$-C$_e$ type twins are asymmetric twins (Fig. S2b). In Twin R_n, every cage on the TP satisfies the mirror symmetry, but the mirror symmetry between the cages over a long distance is not satisfied. The collective orientations of the structural units change once passing through the TP.

To assess the structure-stability relation of the low-energy twinned B$_4$C, we evaluate the energy variations with changing twinning density (Fig. 2d). Rising twinning density causes an obvious energy uptick in Twin A_n structures; meanwhile, Twin S_n series remain nearly degenerate with the single crystal even at the highest twinning density (n=1). The energies of Twin R_n structures become progressively lower than the single crystal as twinning density increases. From another point of view, the newly identified most stable twinned structure (Twin R_1) can be considered as the new lowest-energy crystal structure for B$_4$C. Simulated electronic density of states near the Fermi level (-0.5 to 0.0 eV) of Twin A_1, S_1, and R_1 (Fig. S3), manifest the same sequence as the energy of these twinned structures and also indicate that Twin R_1 contains less high-energy electrons than the other twin structures. The intrinsic strains of various twinned B$_4$C structures are affected by the twin density analogous to those in nanotwinned metals [48–51] and are reflected in their volume changes (Fig. 2e), which correlate well with the corresponding variations of energy (Fig. 2d), showing strain effect on structural relaxation with changing twin density.

The sensitive microstructure dependent energy of twinned B$_4$C showcases two major channels of strain release for structural optimization. The first channel is associated with the alignment of the carbon atom on the icosahedral cage that maximizes the local bonding symmetry with respect to the TP, thus minimizing the strains inside the cages. The rotation of the B$_{11}$C$_p$ cage to align the carbon atoms on the TP optimizes the local bonding symmetry relative to the TP and lowers the energy via strain reduction inside the icosahedral cages, which is responsible for the significantly reduced energy of Twin S_n versus A_n. The second channel is related to the more subtle long-range strains built in the single crystal, that is reduced by breaking the translational symmetry via alternating structural (cage) polarization marked by the position of the carbon atom on the B$_{11}$C$_p$ cage, which further lowers the crystal energy of Twin R_n and brings the energy of the twinned B$_4$C crystal below that of the single crystal (see more discussions about the long-range lattice strain and the short-range atomic strain in the captions of Fig. S2 and bonding structures of Twin A_1, S_1, and R_1 in comparison with R-B$_4$C in the Fig. S4 and Table S4).

Releasing strain energy via paired structural defects with contrasting topological features is known to occur in diverse physical systems, such
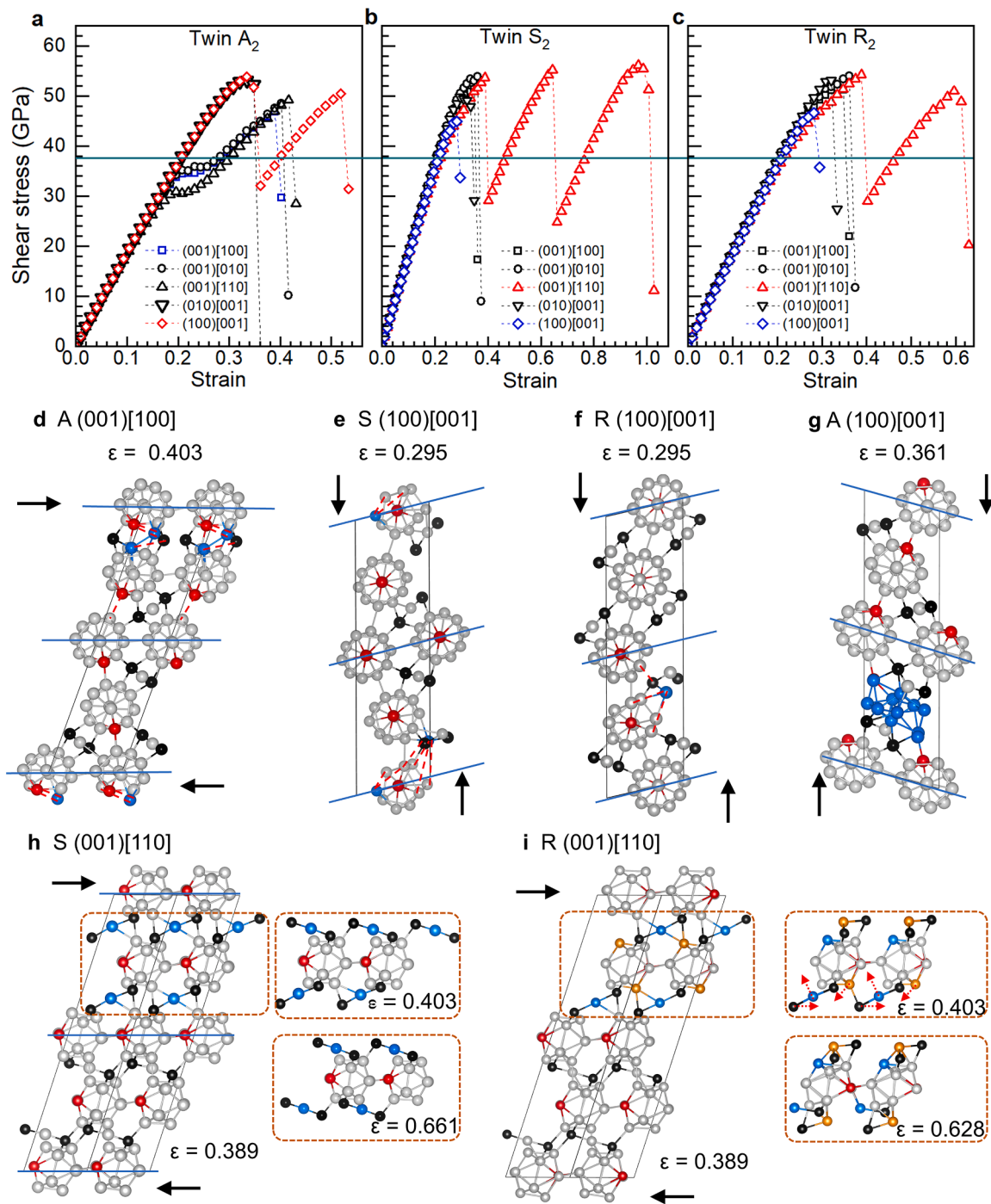
Fig. 3. (a-c) Calculated stress-strain relations in various shear directions. The horizontal green solid bold line represents the ideal shear strength of R-B$_4$C. (d-f) The weakest-shear-direction fracture modes for Twin A$_2$, Twin S$_2$, and Twin R$_2$, respectively. (g-i) The strongest-shear-direction fracture modes for Twin A$_2$, Twin S$_2$, and Twin R$_2$, respectively. The black arrows represent the shear directions. The blue lines are TPs. The broken bonds are shown as red dashed lines and relevant atoms are shown by deep-sky-blue or orange spheres. The carbon atoms from the CBC chains, the carbon atoms from icosahedra, and the boron atoms are represented by black, red, and light gray spheres, respectively. (For interpretation of the references to colour in this figure legend, the reader is referred to the web version of this article.)

as paired dislocations with opposite chirality or handedness in solids and liquid crystals [52–54] or vortex-antivortex pairs in magnets and superconductors [55–59]. These phenomena share the overarching mechanism in that distortions caused by individual defects are effectively compensated by the properly paired defects, thereby reducing the overall disturbance to the system thus lowering the energy cost. The R-B$_4$C hosts an intrinsic microstructural polarization due to the carbon atom incorporation into the boron icosahedron, which produces bonding distortions and the resulting native strains. The alternating stacking pattern with opposite polarization in neighboring matrix and twin parts of Twin R$_n$ crystal alleviates the long-range strain, leading to steadily decreasing energy below the single-crystal value with rising twin density. This finding expands the long-established optimally paired-defect stabilization paradigm to include TB induced strain release, which produces remarkable energetic optimization that is better than the original defect-free system, greatly enriching this prominent class of physical phenomena.
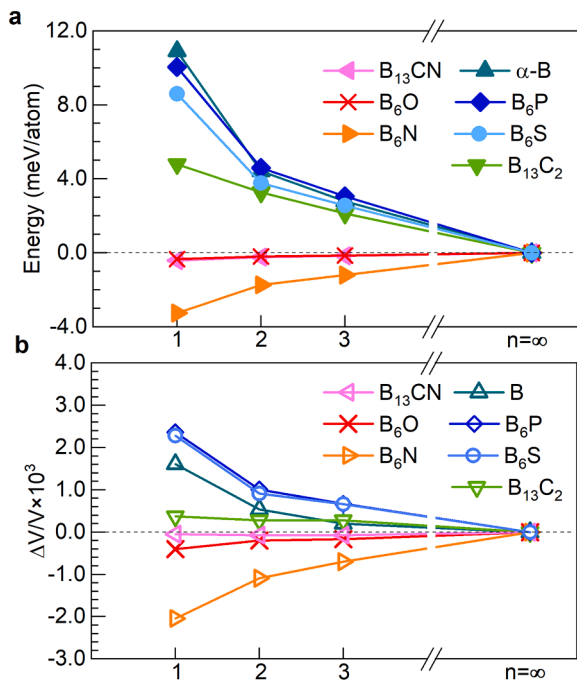
Fig. 4. (a) Calculated energies and (b) volume changes of the twinning structures measured relative to the respective single-crystal results versus slab thickness index n for indicated select boron-rich solids.

3.3. Mechanical properties of twinned B₄C crystals

It's interesting to note that experimental techniques commonly used to reduce defect density and purify single crystal structure, such as thermal annealing, would have the opposite effect here by enhancing the density of twinning phases that have lower energy than the single crystal phase; consequently, pure phase single crystal structures are necessarily unattainable in this class of materials. Instead, specimens obtained under variable synthesis conditions may comprise different degrees of mixture of distinct twinning structures that are energetically close to each other (Figs. S5 and S6), indicating the difficulty of controlling the growth of the stable structure and a single peculiar twinned structure. This is similar to the polytypes in many metal and compound structures. These results enrich the knowledge and understanding of twinning in crystalline solids and provide a unique platform to explore the structure-property relations stemming from the newly identified native microstructural features, which may offer insights into distinct mechanisms governing deformation modes and stress responses (Fig. 3) that dominate structural evolution and dictate mechanical properties, opening unique paths for rational performance tuning and optimization.

The mirror-symmetry Twin S possesses the highest and lowest shear stresses among these three 2-layer-thickness C_p-C_p twin crystals of B₄C under the examined loading strains. TBs hinder shear slips in the single crystal and enhance the ideal shear strength of B₄C by 19.7% (from 37.6 GPa to 45.0 GPa). The CBC chains exhibit obvious deformation and participate in the rearrangements of bonds in the weakest shear stress responses for the three 2-layer-thickness twin crystals of B₄C (Fig. 3d–f). For the failure modes along the strongest shear directions, Twin A exhibits the amorphization of icosahedra (Fig. 3g). It is noted that bond-flip behaviors appear in the strongest shear failure modes of Twin S (see Fig. 3h). The local bond flip can only be captured and identified in the coherent twin structure with an excellent lattice match. In this process (from $\varepsilon = 0.389$ to $\varepsilon = 0.403$ and from $\varepsilon = 0.645$ to $\varepsilon = 0.661$), the icosahedral cage structures are not destroyed and the orientations for part of the CBC chains are changed, which can be considered as a detwinning process. As a result, the strength and ductility of B₄C in this process are increasing accompanied by the change of the twin-boundary

spacing. The stress response of Twin R along the strongest shear direction (Fig. 3i) also exhibits a secondary strengthening attributed to the boron-atom substitution between the distorted CBC chains and adjacent icosahedra. In this process (from $\varepsilon = 0.389$ to $\varepsilon = 0.403$), the icosahedral cage structures also remain intact. The icosahedral cage of Twin R becomes broken with further increase of shear strain.

3.4. Structure and stability of several twinned boron-rich solids

To evaluate twinning stabilization of crystal structure as a broader phenomenon, we further examined a range of boron-rich solids (Fig. 4). A twinned B₁₃CN structure (Fig. S7 and Table S5) is lower in energy than single crystal R-B₁₃CN [60] driven by a rotation-inversion chain configuration at the TB that is effective in releasing the intrinsic strain energy built in the single crystal. For R-B₆N and R-B₆O (Fig. S7 and Table S5), both N and O atoms have smaller atomic radii than B atom and the strong covalent B-N and B-O bonds tighten the distance between the neighboring cages, generating native strains in the single crystal. Twinning modifies the orientation of the B-N and B-O bonds to release the intrinsic strains, thereby lowering the energy to below the rhombohedral single-crystal values. For B₁₃C₂, the BCB chains do not support the rotation-inversion mechanism like B₁₃CN; meanwhile, B₆P and B₆S host large inter-cage distances due to the large atomic radii of P and S atoms and α-B comprises multicenter bonding configurations, all of which do not promote twinning induced strain release. Nevertheless, the close energetic relations indicate that these boron-rich solids also favor multi-domain twinning structures that coexist with the single crystal phase (Fig. S7).

4. Conclusion

In summary, we have developed a method for systematic construction and evaluation of stable twinning structures in complex covalent crystals via selection of energetically favorable twin-boundary orientation and stacking pattern combined with optimization of bonding symmetry of multi-atom structural units relative to the TP. This method has led to the surprising discovery of intrinsically densely twinned structures among icosahedral boron-rich solids, including B₄C, B₁₃CN, B₆O, and B₆N, which are stabler than their respective prevailing single crystals. This discovery establishes a distinct paradigm of defect (twinning) induced stabilization of crystals comprising complex structural units, resulting in multiple domains with variable twinning densities that coexist with the single crystal phase, which is similar to the polytypes in many metal and compound structures.

Declaration of Competing Interest

The authors declare that they have no known competing financial interests or personal relationships that could have appeared to influence the work reported in this paper.

Supplementary materials

Supplementary material associated with this article can be found, in the online version, at doi:10.1016/j.actamat.2023.119151.

References

[1] V. Domnich, S. Reynaud, R.A. Haber, M. Chhowalla, Boron Carbide: Structure, Properties, and Stability under Stress, J. Am. Ceram. Soc. 94 (2011) 3605–3628.

[2] K. Shirai, Electronic structures and mechanical properties of boron and boron-rich crystals (Part I), J. Superhard Mater. 32 (2010) 205–225.

[3] K. Shirai, Electronic structures and mechanical properties of boron and boron-rich crystals (Part II), J. Superhard Mater. 32 (2010) 336–345.

[4] H. Hubert, B. Devouard, L.A.J. Garvie, M.O. Keeffe, P.R. Buseck, W.T. Petuskey, P. F. McMillan, Icosahedral packing of B_{12} icosahedra in boron suboxide (B_6O), Nature 391 (1998) 376–378.

[5] B. Albert, H. Hillebrecht, Boron: elementary challenge for experimenters and theoreticians, Angew. Chem. Int. Ed. 48 (2009) 8640–8668.

[6] H.K. Clark, J.L. Hoard, The crystal structure of boron carbide, J. Am. Chem. Soc. 65 (1943) 2115–2119.

[7] D. Emin, Icosahedral boron-rich solids, Phys. Today 40 (1987) 55–62.

[8] G.H. Kwei, B. Morosin, Structures of the boron-rich boron carbides from neutron powder diffraction: implications for the nature of the inter-icosahedral chains, J. Phys. Chem. 100 (1996) 8031–8039.

[9] R. Lazzari, N. Vast, J.M. Besson, S. Baroni, A.D. Corso, Atomic structure and vibrational properties of icosahedral B_4C boron carbide, Phys. Rev. Lett. 83 (1999) 3230–3233.

[10] N. Vast, J.M. Besson, S. Baroni, A.D. Corso, Atomic structure and vibrational properties of icosahedral α-boron and B_4C boron carbide, Comput. Mater. Sci. 17 (2000) 127–132.

[11] F. Mauri, N. Vast, C.J. Pickard, Atomic structure of icosahedral B_4C boron carbide from a first principles analysis of nmr spectra, Phys. Rev. Lett. 87 (2001), 085506.

[12] A.R. Oganov, C.W. Glass, Crystal structure prediction using *ab initio* evolutionary techniques: Principles and applications, J. Chem. Phys. 124 (2006), 244704.

[13] C.J. Pickard, R.J. Needs, High-pressure phases of silane, Phys. Rev. Lett. 97 (2006), 045504.

[14] Y.C. Wang, J. Lv, L. Zhu, Y.M. Ma, Crystal structure prediction via particle swarm optimization, Phys. Rev. B 82 (2010), 094116.

[15] Y.C. Wang, J. Lv, L. Zhu, Y.M. Ma, CALYPSO: a method for crystal structure prediction, Comput. Phys. Commun. 183 (2012) 2063–2070.

[16] C.J. Pickard, R.J. Needs, *Ab initio* random structure searching, J. Phys. Condens. Matter 23 (2011) 053201.

[17] Q. An, Prediction of superstrong τ-boron carbide phase from quantum mechanics, Phys. Rev. B 95 (2017), 100101.

[18] L.Y. Wang, R.X. Sun, W.H. Liu, Z.K. Yuan, A. Bergara, X.W. Liang, S. Chen, X. F. Zhou, B. Xu, J.L. He, D.L. Yu, G.Y. Gao, Y.J. Tian, Novel superhard boron-rich nitrides under pressure, Sci. China Mater. 63 (2020) 2358–2364.

[19] Q. An, K.M. Reddy, H.F. Dong, M.W. Chen, A.R. Oganov, W.A. Goddard III, Nanotwinned Boron Suboxide (B_6O): New Ground State of B_6O, Nano Lett. 16 (2016) 4236–4242.

[20] K. Lu, Stabilizing nanostructures in metals using grain and twin boundary architectures, Nat. Rev. Mater. 1 (2016) 1.

[21] E.M. Heian, S.K. Khalsa, J.W. Lee, Z.A. Munir, T. Yamamoto, M. Ohyanagi, Synthesis of dense, high-defect-concentration B_4C through mechanical activation and field-assisted combustion, J. Am. Ceram. Soc. 87 (2004) 779–783.

[22] U. Anselmi-Tamburiniw, Z.A. Munir, Y. Kodera, T. Imai, M. Ohyanagi, Influence of synthesis temperature on the defect structure of boron carbide: experimental and modeling studies, J. Am. Ceram. Soc. 88 (2005) 1382–1387.

[23] B. Chang, B.L. Gersten, S.T. Szewczyk, J.W. Adams, Characterization of boron carbide nanoparticles prepared by a solid state thermal reaction, Appl. Phys. A 86 (2007) 83–87.

[24] M.F. Toksoy, W. Rafaniello, K.Y. Xie, L. Ma, K.J. Hemker, R.A. Haber, Densification and characterization of rapid carbothermal synthesized boron carbide, Int. J. Appl. Ceram. Technol. 14 (2017) 443–453.

[25] P.H. Li, M.D. Ma, Y.J. Wu, X. Zhang, Y.K. Chang, Z.W. Zhuge, L. Sun, W.T. Hu, D. Yu, B. Xu, Z.S. Zhao, J.Y. Chen, J.L. He, Y.J. Tian, Preparation of dense B_4C ceramics by spark plasma sintering of high-purity nanoparticles, J. Eur. Ceram. Soc. 41 (2021) 3929–3936.

[26] P.H. Li, Y.Q. Bu, L.Y. Wang, C. Wang, J.Q. Huang, K. Tong, Y.J. Chen, J.L. He, Z. S. Zhao, B. Xu, Z.Y. Liu, G.Y. Gao, A.M. Nie, H.T. Wang, Y.J. Tian, *In situ* observation of fracture along twin boundaries in boron carbide, Adv. Mater. 2204375 (2022) 1–7.

[27] T. Fujita, P. Guan, K.M. Reddy, A. Hirata, J. Guo, M. Chen, Asymmetric twins in rhombohedral boron carbide, Appl. Phys. Lett. 104 (2014), 021907.

[28] K.Y. Xie, Q. An, M.F. Toksoy, R.A. Haber, W.A. Goddard III, K.J. Hember, Atomic-level understanding of "asymmetric twins" in boron carbide, Phys. Rev. Lett. 115 (2015), 175501.

[29] Q. An, W.A. Goddard III, Atomistic origin of brittle failure of boron carbide from large-scale reactive dynamics simulations: suggestions toward improved ductility, Phys. Rev. Lett. 115 (2015), 105501.

[30] Q. An, W.A. Goddard III, K.Y. Xie, G. Sim, K.J. Hemker, T. Munhollon, M.F. Toksoy, R.A. Haber, Superstrength through Nanotwinning, Nano Lett. 16 (2016) 7573–7579.

[31] X.K. Yang, S.P. Coleman, J.C. Lasalvia, W.A. Goddard, Q. An, Shear-induced brittle failure along grain boundaries in boron carbide, ACS Appl. Mater. Interfaces 10 (2018) 5072–5080.

[32] Q. An, K.M. Reddy, K.Y. Xie, K.J. Hemker, W.A. Goddard III, New ground-state crystal structure of elemental boron, Phys. Rev. Lett. 117 (2016), 085501.

[33] Q. An, K.M. Reddy, J. Qian, K.J. Hemker, M.W. Chen, W.A. Goddard III, Nucleation of amorphous shear bands at nanotwins in boron suboxide, Nat. Commun. 7 (2016) 11001.

[34] Y.J. Tian, B. Xu, D.L. Yu, Y.M. Ma, Y.B. Wang, Y.B. Jiang, W.T. Hu, C.C. Tang, Y. F. Gao, K. Luo, Z.S. Zhao, L.M. Wang, B. Wen, J.L. He, Z.Y. Liu, Ultrahard nanotwinned cubic boron nitride, Nature 493 (2013) 385–388.

[35] B. Li, H. Sun, C.F. Chen, Large indentation strain stiffening in nanotwinned cubic boron nitride, Nat. Commun. 5 (2014) 4965.

[36] Q. Huang, D.L. Yu, B. Xu, W.T. Hu, Y.M. Ma, Y.B. Wang, Z.S. Zhao, B. Wen, J.L. He, Z.Y. Liu, Y.J. Tian, Nanotwinned diamond with unprecedented hardness and stability, Nature 510 (2014) 250–253.

[37] B. Li, H. Sun, C.F. Chen, Extreme mechanics of probing the ultimate strength of nanotwinned diamond, Phys. Rev. Lett. 117 (2016), 116103.

[38] D.M. Ceperley, B.J. Alder, Ground state of the electron gas by a stochastic method, Phys. Rev. Lett. 45 (1980) 566–569.

[39] J.P. Perdew, A. Zunger, Self-interaction correction to density-functional approximations for many-electron systems, Phys. Rev. B 23 (1981) 5048–5079.

[40] G. Kresse, L. Furthmüller, Efficient iterative schemes for *ab initio* total-energy calculations using a plane-wave basis set, Phys. Rev. B 54 (1996) 11169–11186.

[41] G. Kresse, J. Joubert, From ultrasoft pseudopotentials to the projector augmented-wave method, Phys. Rev. B 59 (1999) 1758–1775.

[42] H.J. Monkhorst, J.D. Pack, Special points for Brillouin-zone integrations, Phys. Rev. B 13 (1976) 5188–5192.

[43] A. Togo, F. Oba, I. Tanaka, First-principles calculations of the ferroelastic transition between rutile-type and $CaCl_2$-type SiO_2 at high pressures, Phys. Rev. B 78 (2008), 134106.

[44] Y. Zhang, H. Sun, C.F. Chen, Superhard cubic BC_2N compared to diamond, Phys. Rev. Lett. 93 (2004), 195504.

[45] C. Liu, X.Q. Song, Q. Li, Y.M. Ma, C.F. Chen, Smooth flow in diamond: atomistic ductility and electronic conductivity, Phys. Rev. Lett. 123 (2019), 195504.

[46] C. Liu, X.L. Gu, K. Zhang, W.T. Zheng, Y.M. Ma, C.F. Chen, Superhard metallic compound TaB_2 via crystal orientation resolved strain stiffening, Phys. Rev. B 105 (2022), 024105.

[47] X.Q. Song, C. Liu, Q. Li, Y.M. Ma, C.F. Chen, Stress-induced high-T_c superconductivity in solid molecular hydrogen, Proc. Natl. Acad. Sci. U. S. A. 119 (2022), e2122691119.

[48] Q.S. Pan, L. Lu, Strain-controlled cyclic stability and properties of Cu with highly oriented nanoscale twins, Acta Mater. 81 (2014) 248–257.

[49] R.T. Ott, J. Geng, M.F. Besser, M.J. Kramer, Y.M. Wang, E.S. Park, R. LeSar, A. H. King, Optimization of strength and ductility in nanotwinned ultra-fine grained Ag: Twin density and grain orientations, Acta Mater. 96 (2015) 378–389.

[50] M. Wang, X.Y. Xu, H.Y. Wang, L.H. He, M.X. Huang, Evolution of dislocation and twin densities in a Mg alloy at quasi-static and high strain rates, Acta Mater. 201 (2020) 102–113.

[51] Y.A. Sun, Z.P. Luo, X.Y. Li, K. Lu, Effects of stacking fault energy on deformation induced grain boundary relaxation in nanograined Cu alloys, Acta Mater. 239 (2022), 118256.

[52] M. Kleman, J. Friedel, Disclinations, dislocations, and continuous defects: a reappraisal, Rev. Mod. Phys. 80 (2008) 61–115.

[53] P. Pieranski, Dislocations and other topological oddities, C. R. Phys. 17 (2016) 242–263.

[54] A. Repula, E. Grelet, Elementary edge and screw dislocations visualized at the lattice periodicity level in the smectic phase of colloidal rods, Phys. Rev. Lett. 121 (2018), 097801.

[55] R. Geurts, M.V. Milošević, F.M. Peeters, Symmetric and asymmetric vortex-antivortex molecules in a fourfold superconducting geometry, Phys. Rev. Lett. 97 (2006), 137002.

[56] J.S. Neal, M.V. Milošević, S.J. Bending, A. Potenza, L. San Emeterio, C.H. Marrows, Competing symmetries and broken bonds in superconducting vortex-antivortex molecular crystals, Phys. Rev. Lett. 99 (2007), 127001.

[57] M. Iavarone, A. Scarfato, F. Bobba, M. Longobardi, G. Karapetrov, V. Novosad, V. Yefremenko, F. Giubileo, A.M. Cucolo, Imaging the spontaneous formation of vortex-antivortex pairs in planar superconductor/ferromagnet hybrid structures, Phys. Rev. B 84 (2011), 024506.

[58] F.N. Rybakov, A. Pervishko, O. Eriksson, E. Babaev, Antichiral ferromagnetism, Phys. Rev. B 104 (2021) L020406.

[59] S.K. Karna, M. Marshall, W. Xie, L. DeBeer-Schmitt, D.P. Young, I. Vekhter, W. A. Shelton, A. Kovács, M. Charilaou, J.F. DiTusa, Annihilation and control of chiral domain walls with magnetic Fields, Nano Lett. 21 (2021) 1205–1212.

[60] H. Liang, Q. Li, C.F. Chen, Atomistic mechanisms for contrasting stress-strain relations of $B_{13}CN$ and $B_{13}C_2$, J. Phys. Chem. Lett. 11 (2020) 10454–10462.

Supplementary materials for:
Intrinsic Dense Twinning via Release of Native Strain

Xianqi Song,[1, #] Chang Liu,[1, 2, #] Quan Li,[1, 2, *] Yanming Ma,[1, 2, *] and Changfeng Chen[3, *]

[1] State Key Lab of Superhard Materials and Key Laboratory of Material Simulation Methods & Software of Ministry of Education, College of Physics, Jilin University, Changchun 130012, China

[2] International Center of Future Science, Jilin University, Changchun 130012, China

[3] Department of Physics and Astronomy, University of Nevada, Las Vegas, Nevada 89154, USA

[#]These authors contributed equally: Xianqi Song (X.Q. Song), Chang Liu (C. Liu)

*Corresponding author.
Email address: liquan777@jlu.edu.cn (Q. Li); mym@jlu.edu.cn (Y.M. Ma); changfeng.chen@unlv.edu (C.F. Chen).

Structural snapshots for twinned B_4C in different crystal orientations, the energy and structure of C_p-C_e Twin and stacking fault of R-B_4C, density of states for the 1-layer-thick B_4C twinning structures, dynamic stability of Twin B_4C structures, theoretically simulated or experimentally observed XRD of B_4C, bond lengths in the icosahedral cages of the single crystal and 1-layer-thick B_4C twinning structures, and structural information for the 1-, 2-, and 3-layer-thick B_4C twinning structures and the twinned B_6N, $B_{13}CN$, and B_6O structures.

This file includes:

Figures S1-S7

Tables S1-S5
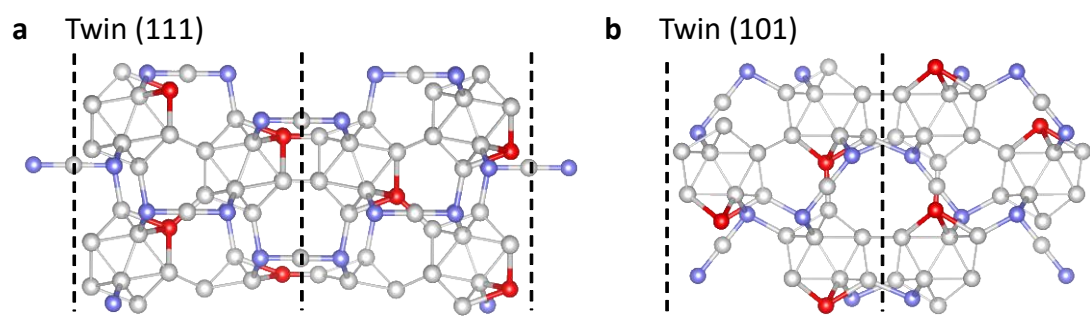
Fig. S1. **The twinned crystals of B₄C.** The twinned B$_4$C crystals with **a** (111) and **b** (101) oriented twin planes, which are marked by the vertical dashed lines. The carbon atoms on the CBC chains, on the icosahedra, and the boron atoms are represented by lavender, red, and gray spheres, respectively.
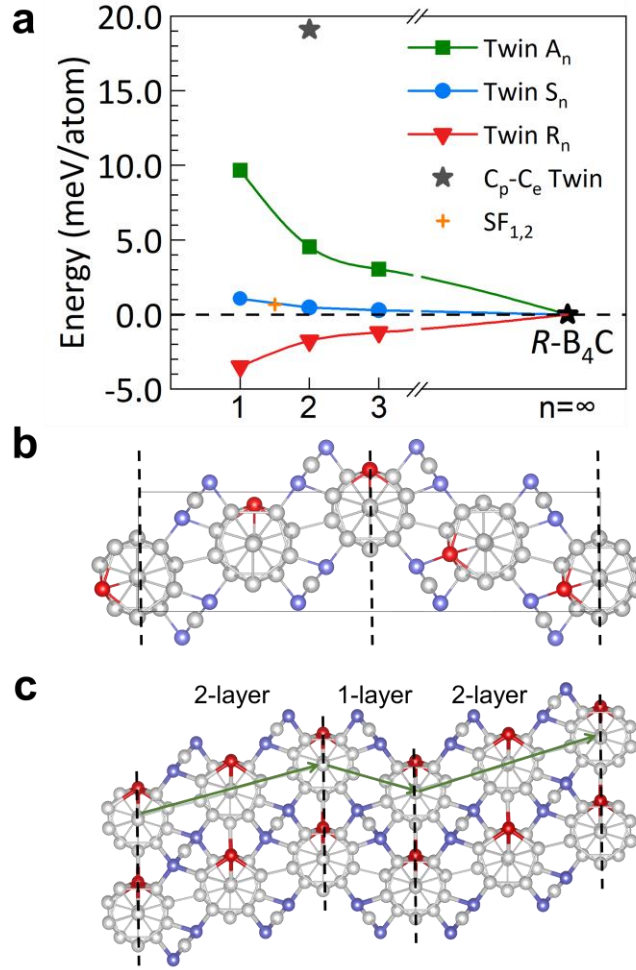
Fig. S2. The energy and structure of C_p-C_e Twin and stacking fault (SF) of R-B_4C. a Energies relative to the single crystal values, which are set to zero. **b** the C_p-C_e type twinned structure and **c** stacking fault structure, where boron atoms, carbon atoms on CBC chains and carbon atoms on icosahedra are represented by gray, lavender and red spheres, respectively. The long-range lattice strain and the short-range atomic strain usually appear simultaneously. The influence of long-range lattice strain on energy is mainly contributed by twin density and collective orientations of the structural units. The short-range atomic strain is dominated by local bonding connections at the twin boundary and the change of chemical bonding types in the matrix or twin part in twin structures. Combined with data in Fig. 2d, we quantitatively estimate the strain energies under these different conditions based on the microstructural arrangements, and the results show the following sequence: twin density (< 1 meV, compared with R-B_4C and Twin S_n) < collective orientations of structural units (about 2-5 meV, compared with Twin R_n and Twin S_n) < local bonding connection at the twin boundary (about 3-9 meV, compared with Twin A_n and Twin S_n) < change of chemical bonding types in matrix or twin part in twin structures (>10 meV, compared with C_p-C_p Twin and C_p-C_e Twin). These estimates are obtained by a systematic comparison of calculated energetic data. Specifically, the effect of twin density comes from comparing the

energies of the single crystal R-B$_4$C and Twin S_n (n=1,2,3,…), where the largest difference between R-B$_4$C and Twin S_1 is less than 1 meV; the effect of collective orientations of structural units is obtained by comparing the energies of Twin R_3 and S_3, which is 2 meV, and those of Twin R_1 and S_1, which is 5 meV; the effect of local bonding connection at the twin boundary is obtained by comparing the energies of Twin A_3 and S_3, which is 3 meV, and those Twin A_1 and S_1, which is 9 meV; and finally, the effect of change of chemical bonding types in matrix or twin part in twin structures is estimated by comparing the energies of C_p-C_e twin and Twin A_1, which is more than 10 meV, and those of C_p-C_e twin and other Twin A_n, which is even larger. Stacking faults in B$_4$C are often generated simultaneously with twins in experiments and their structures are closely related to twin structures. Here, we have constructed a stacking fault (SF) on the (010) plane of R-B$_4$C, termed SF$_{1,2}$, and this structure similar to gradient twin can be seen as a combination of the matrix part in Twin S_1 and the twin part in Twin S_2. The energy of this stacking fault lies in between those for Twin S_1 and Twin S_2.
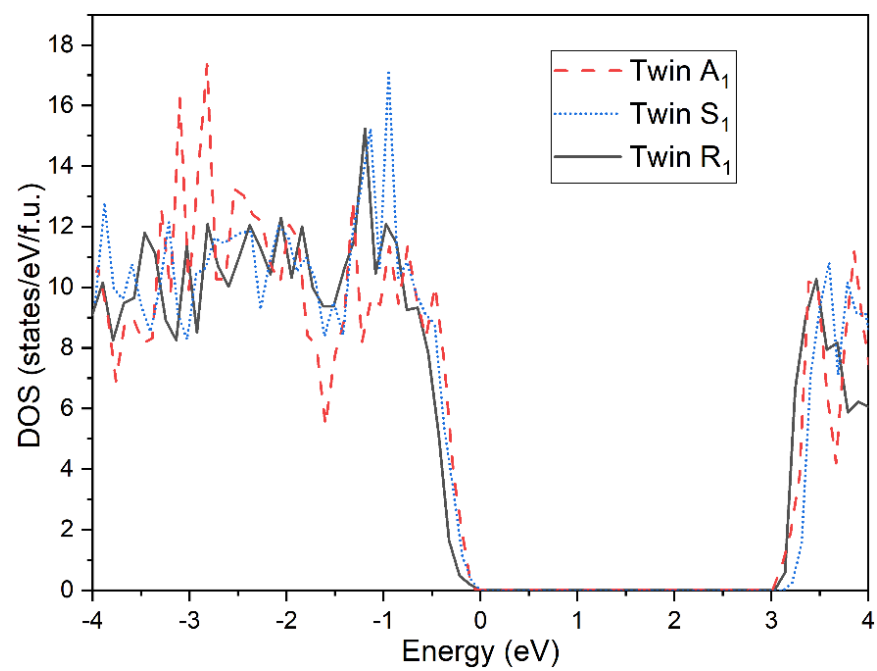
Fig. S3. Electronic density of states (DOS) for Twin A_1, Twin S_1, and Twin R_1.
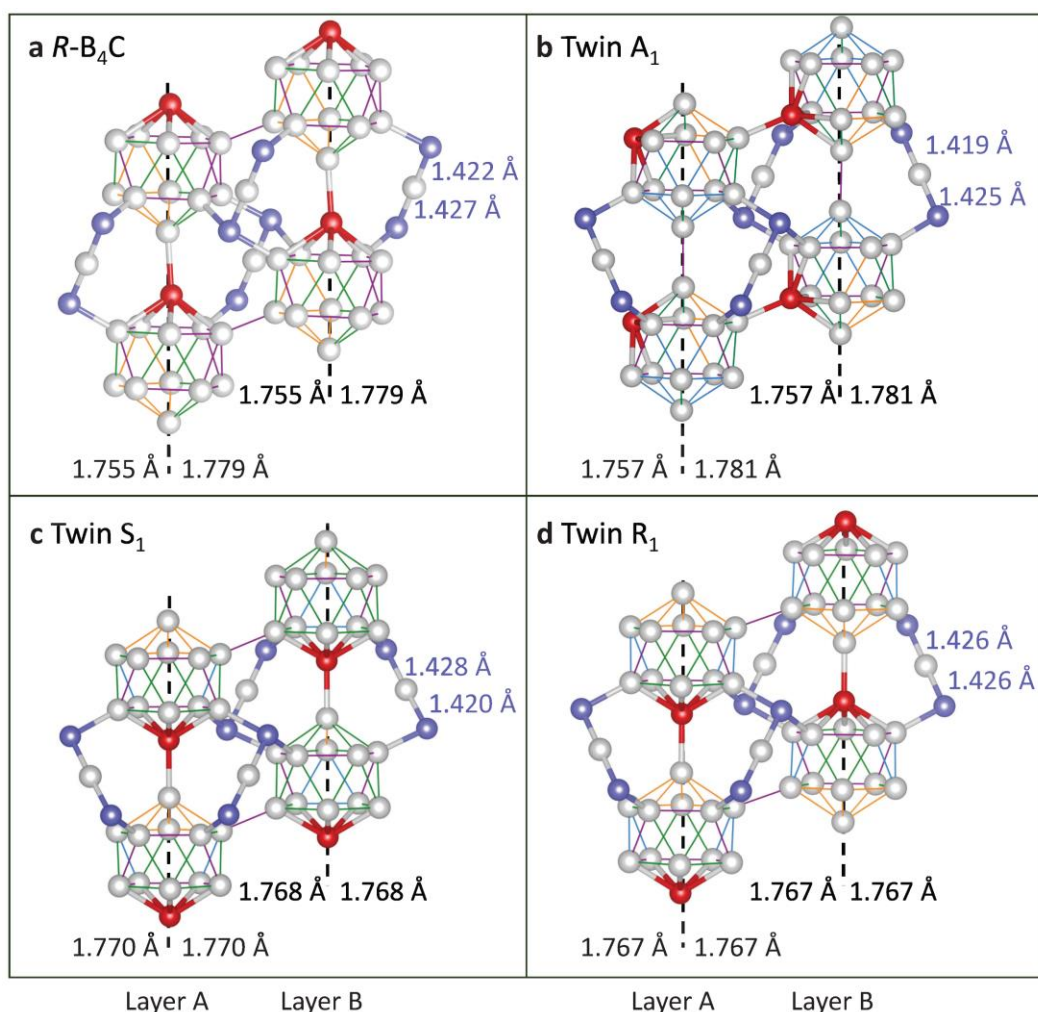
Fig. S4. Bonding configurations of (a) *R*-B$_4$C, (b) Twin A$_1$, (c) Twin S$_1$, and (d) Twin R$_1$. The C-B bonds and B-B bonds are represented by bicolor thick lines and unicolor thin lines, respectively. The purple, blue, green, and orange thin lines represent the length of B-B bonds in the range of <1.750, 1.750−1.770, 1.770−1.790, and >1.790 Å, respectively. The listed values are the average bond lengths on the left and right halves of the B$_{11}$C cages in the two distinct stacking layers and those on the adjacent CBC chain (Table S4). The vertical dashed lines represent the (010) plane in single crystal and TPs in twinned crystal structures. The single crystal hosts an inhomogeneous distribution of bond lengths throughout the structural units. The average bond lengths on the two halves of the icosahedral B$_{11}$C cage are notably different and so are the B-C bond lengths on the CBC chain, all of which indicate the presence of considerable native strains that cause bonding distortions. Twin A$_1$ possesses nearly identical bond-length disparities, reflecting similar amount and extent of native strains in the crystal, but the average bond lengths on the cage is slightly longer, leading to the higher energy compared to the single crystal. With the rotational adjustment aligning the on-cage carbon atoms inside the TPs, Twin S$_1$ hosts a more symmetric bonding arrangement relative to the TP, with identical average bond lengths on the two halves of each cage, but the results on cages in adjacent layers are different and the C-B bonds on the CBC chain also

have different lengths, indicating reduced but residual strains in the crystal structure. Finally, after adjusting the adjacent cages by alternating the alignments of the carbon-atom dictated structural polarization of the cages in neighboring slabs, Twin R_1 exhibits fully symmetric bonding arrangements with identical average bond lengths on the two halves of every cage and the same C-B bond lengths on the CBC chain throughout the crystal, indicating the effective removal of native strains originally built in the single crystal. This symmetry guided strain release creates a fully relaxed crystal with energy lower than the single crystal.
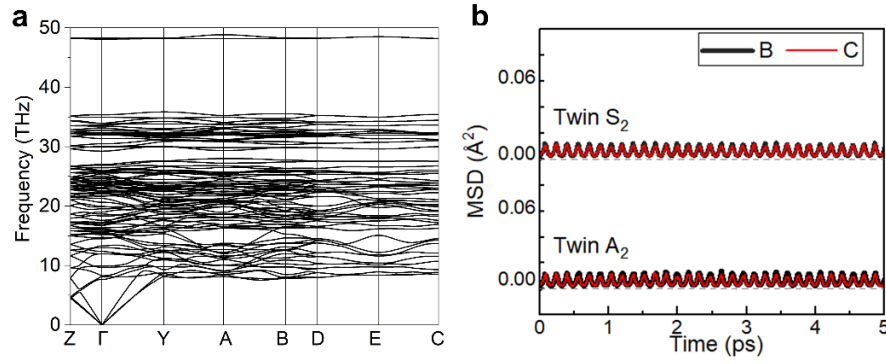
Fig. S5. Dynamic stability of Twin B₄C structures. a Calculated phonon dispersion curves of Twin R_1 ($P2_1/m$ space group symmetry) at 0 K demonstrate dynamic stability of this newly discovered low-energy structure. **b** Simulated atomic mean-square displacements (MSDs) of Twin S_2 and Twin A_2 structures by *ab initio* molecular dynamics show that these metastable structures remain stable at 300 K, indicating that twin structures Twin A_n, S_n, R_n with variable twinning densities may coexist in the sample.
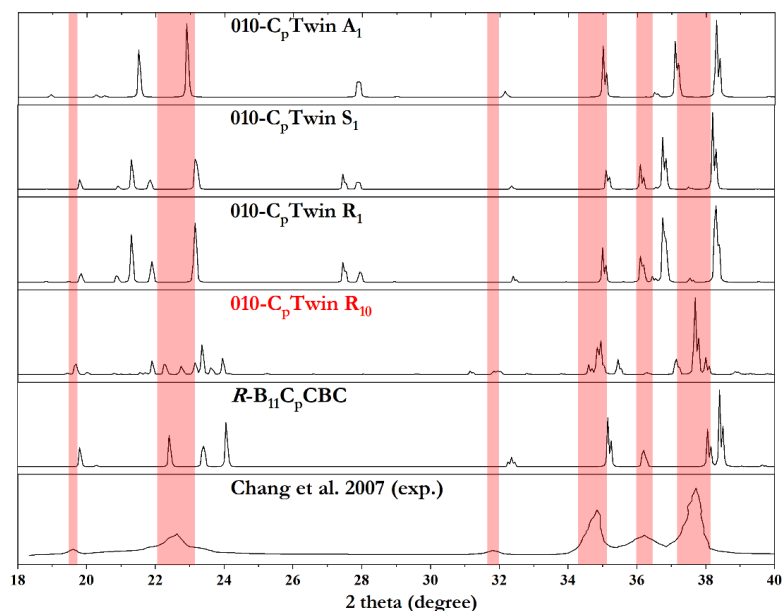
Fig. S6. Theoretically simulated and experimentally observed XRD of B₄C. According to the principle of minimum energy, reactants tend to form the most thermodynamically stable product; however, metastable products at local free energy minima are often obtained during synthesis, and these metastable structures are usually separated by well-defined phase boundaries and impeded by kinetic barriers along the pathway toward the thermodynamic equilibrium. Our calculations show that the energy difference between the twin structure Twin R_{10} (twin plane spacing d=4.5 nm) and single crystal R-B₄C (n=∞) is less than 1 meV/atom, which gives similar synthesis probability and potential phase coexistence of multi-density twins due to their close energetics. In fact, twin structures with diverse atomic arrangements and density of twins are often observed in the synthesized samples via various reactant quality and reaction pathways. This point has been strongly supported by the previous relevant experimental data of B₄C, e.g. (1) the inevitable nano-twins and stacking faults are shown in the commercial hot-pressed powders of B₄C [1]; (2) all rapid carbothermal reduction particles are observed to contain high-density nanotwins. Generally speaking, the smaller the particle, the higher the twin density. The twins are observed only a few nanometers apart in the small particles (~200 nm) and tens of nanometers apart in larger particles (~800 nm) [2]; (3) the high-density twinning samples with polytypic microstructures of B₄C have also been widely synthesized and observed in the previous experimental studies [3-7]. These experiments indicate that the synthesis avenues have a crucial influence on the density and microstructure of twins. By the comparison of simulated XRD results for Twin A_1, S_1, R_1, and relative low-density Twin R_{10} with the experimental XRD (Cu K_α) of boron carbide with dense twins [4], the results indicate that single crystal and twin structures of Twin A_n, S_n, R_n with variable twinning densities may coexist in the sample. It is possible that other energetically competitive twinning patterns also appear in some cases. These extraordinary material behaviors expand the textbook description of the effect of twinning on crystal stability and define a distinct category of intrinsically nanotwinned materials.

a a-B

b B$_{13}$C$_2$

c B$_{13}$CN

d B$_6$X (X=N, O, P, S)

Single crystal   Twinned crystal (n=2)
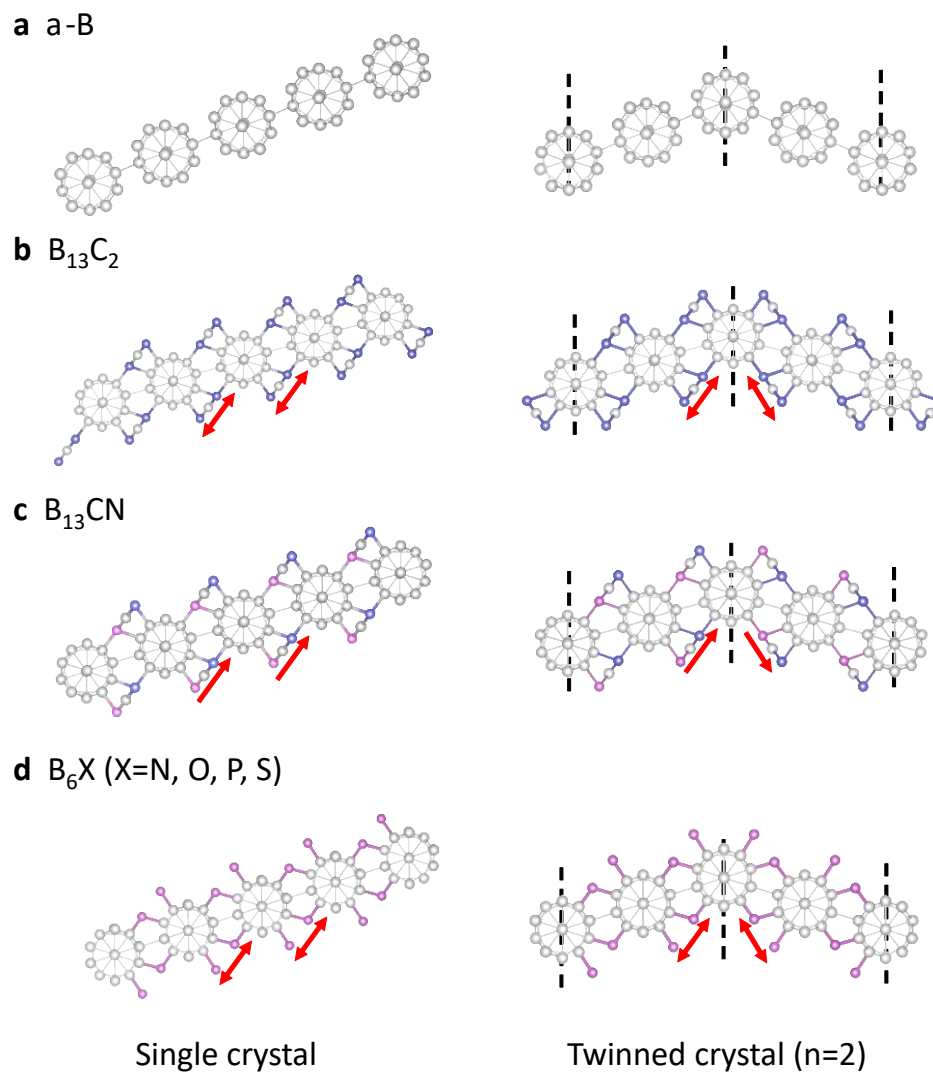
Fig. S7. Structural snapshots of the single crystal (left) and twinned crystal (right) structures of selected boron-rich solids containing icosahedral cages. The N (and O, P, S), C, and B atoms are represented by pink, lavender, and gray spheres, respectively. The vertical dashed lines represent the TPs. The red double-headed arrows indicate the orientation and symmetry of the 3-atom chains or distribution of the X atom in the single crystal and twinned crystal of selected boron-rich solids.

TABLE S1. Calculated lattice constants and atomic coordinates for the 1-layer-thick twinned B_4C.

Parameter (Å, °)	Twin A_1			Twin S_1			Twin R_1		
	$a =$ 5.145	$b =$ 5.145	$c =$ 8.759	$a =$ 5.145	$b =$ 4.992	$c =$ 8.961	$a =$ 5.160	$b =$ 4.987	$c =$ 8.949
	$\alpha =$ 90.000	$\beta =$ 90.000	$\gamma =$ 65.486	$\alpha =$ 90.000	$\beta =$ 90.000	$\gamma =$ 66.179	$\alpha =$ 90.000	$\beta =$ 90.000	$\gamma =$ 65.960
Atoms	x	y	z	x	y	z	x	y	z
B1	0.169	0.678	0.899	0.183	0.685	0.901	0.182	0.679	0.901
B2	0.032	0.032	0.657	0.330	0.319	0.835	0.328	0.313	0.835
B3	0.678	0.169	0.899	0.025	0.028	0.656	0.028	0.034	0.656
B4	0.238	0.238	0.668	0.688	0.171	0.900	0.686	0.163	0.900
B5	0.524	0.524	0.836	0.232	0.238	0.662	0.231	0.246	0.660
B6	0.386	0.881	0.596	0.533	0.533	0.840	0.531	0.525	0.840
B7	0.881	0.386	0.596	0.376	0.874	0.594	0.377	0.880	0.594
B8	0.774	0.774	0.745	0.875	0.388	0.595	0.873	0.397	0.595
B9	0.174	0.678	0.096	0.777	0.771	0.747	0.780	0.780	0.748
B10	0.321	0.321	0.168	0.183	0.685	0.094	0.182	0.679	0.094
B11	0.036	0.036	0.336	0.330	0.319	0.160	0.328	0.313	0.160
B12	0.807	0.128	0.495	0.025	0.028	0.339	0.028	0.034	0.340
B13	0.093	0.414	0.998	0.799	0.119	0.498	0.798	0.127	0.498
B14	0.678	0.174	0.096	0.109	0.413	0.998	0.104	0.410	0.998
B15	0.527	0.527	0.157	0.688	0.171	0.096	0.686	0.163	0.095
B16	0.145	0.466	0.498	0.232	0.238	0.334	0.231	0.246	0.335
B17	0.431	0.752	0.995	0.533	0.533	0.155	0.531	0.525	0.156
B18	0.390	0.881	0.399	0.137	0.474	0.498	0.136	0.482	0.498
B19	0.466	0.145	0.498	0.440	0.772	0.998	0.377	0.880	0.401
B20	0.752	0.431	0.995	0.376	0.874	0.401	0.455	0.149	0.498
B21	0.881	0.390	0.399	0.455	0.143	0.498	0.761	0.432	0.998
B22	0.785	0.785	0.245	0.765	0.437	0.998	0.873	0.397	0.400
B23	0.414	0.093	0.998	0.875	0.388	0.401	0.780	0.780	0.248
B24	0.128	0.807	0.495	0.777	0.771	0.249	0.424	0.077	0.998
C1	0.325	0.325	0.839	0.428	0.105	0.998	0.438	0.743	0.998
C2	0.234	0.234	0.339	0.119	0.811	0.498	0.121	0.817	0.498
C3	0.927	0.927	0.805	0.934	0.923	0.808	0.944	0.925	0.808
C4	0.621	0.621	0.686	0.615	0.626	0.683	0.615	0.635	0.688
C5	0.938	0.938	0.186	0.934	0.923	0.187	0.944	0.925	0.188
C6	0.632	0.632	0.305	0.615	0.626	0.313	0.615	0.635	0.308

TABLE S2. Calculated lattice constants and atomic coordinates for the 2-layer-thick twinned B_4C.

	Twin A_2			Twin S_2			Twin R_2		
Parameter (Å, °)	$a =$ 5.146	$b =$ 5.146	$c =$ 17.510	$a =$ 5.146	$b =$ 4.991	$c =$ 17.920	$a =$ 5.153	$b =$ 4.988	$c =$ 17.908
	$\alpha =$ 90.000	$\beta =$ 90.000	$\gamma =$ 65.303	$\alpha =$ 90.000	$\beta =$ 90.000	$\gamma =$ 66.148	$\alpha =$ 90.000	$\beta =$ 90.000	$\gamma =$ 66.046
Atoms	x	y	z	x	y	z	x	y	z
B1	0.416	0.096	0.747	0.731	0.055	0.000	0.120	0.475	0.500
B2	0.699	0.376	0.000	0.122	0.468	0.500	0.216	0.240	0.581
B3	0.137	0.815	0.499	0.427	0.761	0.752	0.522	0.517	0.832
B4	0.174	0.684	0.701	0.217	0.232	0.582	0.668	0.151	0.798
B5	0.451	0.964	0.950	0.523	0.521	0.832	0.361	0.874	0.548
B6	0.041	0.041	0.580	0.667	0.158	0.798	0.516	0.518	0.671
B7	0.320	0.320	0.829	0.361	0.868	0.548	0.825	0.807	0.921
B8	0.815	0.137	0.499	0.518	0.525	0.672	0.671	0.155	0.701
B9	0.096	0.416	0.747	0.823	0.816	0.921	0.978	0.446	0.952
B10	0.376	0.699	0.000	0.672	0.163	0.701	0.440	0.143	0.500
B11	0.684	0.174	0.701	0.980	0.453	0.951	0.744	0.424	0.751
B12	0.964	0.451	0.950	0.440	0.137	0.500	0.053	0.715	0.000
B13	0.247	0.247	0.584	0.748	0.428	0.751	0.073	0.066	0.875
B14	0.525	0.525	0.836	0.056	0.720	0.000	0.765	0.773	0.625
B15	0.529	0.529	0.671	0.067	0.053	0.874	0.783	0.120	0.500
B16	0.806	0.806	0.919	0.764	0.763	0.625	0.087	0.401	0.749
B17	0.713	0.036	0.999	0.783	0.113	0.500	0.396	0.692	1.000
B18	0.152	0.475	0.500	0.092	0.404	0.749	0.858	0.390	0.549
B19	0.433	0.756	0.752	0.399	0.696	0.000	0.163	0.666	0.799
B20	0.673	0.167	0.799	0.859	0.382	0.548	0.013	0.027	0.579
B21	0.395	0.888	0.550	0.165	0.672	0.799	0.318	0.303	0.828
B22	0.475	0.152	0.500	0.011	0.021	0.579	0.167	0.672	0.702
B23	0.756	0.433	0.752	0.317	0.311	0.829	0.475	0.962	0.952
B24	0.036	0.713	0.999	0.169	0.677	0.702	0.313	0.306	0.668
B25	0.888	0.395	0.550	0.474	0.969	0.952	0.619	0.597	0.918
B26	0.167	0.673	0.799	0.314	0.312	0.668	0.426	0.768	0.248
B27	0.057	0.057	0.872	0.621	0.601	0.919	0.216	0.238	0.418
B28	0.782	0.782	0.624	0.427	0.761	0.248	0.522	0.529	0.168
B29	0.418	0.095	0.252	0.217	0.232	0.418	0.668	0.164	0.202
B30	0.177	0.683	0.299	0.523	0.521	0.168	0.361	0.874	0.452
B31	0.456	0.963	0.050	0.667	0.158	0.202	0.517	0.532	0.328
B32	0.325	0.325	0.336	0.361	0.868	0.452	0.823	0.808	0.079

B33	0.604	0.604	0.084	0.518	0.525	0.328	0.672	0.169	0.299
B34	0.044	0.044	0.419	0.823	0.816	0.079	0.978	0.445	0.049
B35	0.321	0.321	0.171	0.672	0.163	0.299	0.748	0.434	0.249
B36	0.095	0.418	0.252	0.98	0.453	0.049	0.070	0.062	0.125
B37	0.683	0.177	0.299	0.748	0.428	0.249	0.762	0.769	0.375
B38	0.963	0.456	0.050	0.067	0.053	0.126	0.091	0.411	0.251
B39	0.531	0.531	0.329	0.764	0.763	0.375	0.858	0.389	0.452
B40	0.810	0.810	0.080	0.092	0.404	0.251	0.164	0.680	0.201
B41	0.434	0.754	0.247	0.859	0.382	0.452	0.010	0.028	0.421
B42	0.677	0.166	0.201	0.165	0.672	0.201	0.319	0.317	0.171
B43	0.399	0.887	0.450	0.011	0.021	0.421	0.167	0.684	0.298
B44	0.754	0.434	0.247	0.317	0.311	0.171	0.474	0.962	0.048
B45	0.887	0.399	0.450	0.169	0.677	0.298	0.314	0.318	0.332
B46	0.166	0.677	0.201	0.474	0.969	0.048	0.619	0.595	0.081
B47	0.068	0.068	0.124	0.314	0.312	0.332	0.410	0.067	0.748
B48	0.793	0.793	0.372	0.621	0.601	0.081	0.715	0.360	1.000
C1	0.331	0.331	0.669	0.411	0.096	0.748	0.731	0.025	0.000
C2	0.608	0.608	0.921	0.719	0.388	0.000	0.424	0.733	0.751
C3	0.242	0.242	0.421	0.104	0.804	0.500	0.104	0.810	0.500
C4	0.519	0.519	0.169	0.600	0.620	0.593	0.599	0.629	0.595
C5	0.211	0.211	0.902	0.905	0.910	0.843	0.915	0.914	0.845
C6	0.936	0.936	0.654	0.225	0.205	0.905	0.236	0.209	0.907
C7	0.629	0.629	0.596	0.921	0.916	0.655	0.931	0.917	0.655
C8	0.903	0.903	0.844	0.411	0.096	0.252	0.412	0.102	0.251
C9	0.221	0.221	0.096	0.600	0.620	0.407	0.599	0.627	0.407
C10	0.947	0.947	0.344	0.905	0.910	0.157	0.904	0.918	0.155
C11	0.640	0.640	0.402	0.225	0.205	0.095	0.236	0.207	0.095
C12	0.915	0.915	0.154	0.921	0.916	0.345	0.920	0.922	0.345

TABLE S3. Calculated lattice constants and atomic coordinates for the 3-layer-thick twinned B$_4$C.

Parameter (Å, °)	Twin A$_3$			Twin S$_3$			Twin R$_3$		
	$a =$ 5.147	$b =$ 5.147	$c =$ 26.265	$a =$ 5.146	$b =$ 4.991	$c =$ 26.879	$a =$ 5.151	$b =$ 4.989	$c =$ 26.867
	$\alpha =$ 90.000	$\beta =$ 90.000	$\gamma =$ 65.248	$\alpha =$ 90.000	$\beta =$ 90.000	$\gamma =$ 66.141	$\alpha =$ 90.000	$\beta =$ 90.000	$\gamma =$ 66.072
Atoms	x	y	z	x	y	z	x	y	z
B1	0.698	0.021	0.999	0.739	0.054	0.000	0.821	0.185	0.500
B2	0.860	0.183	0.500	0.822	0.178	0.500	0.222	0.228	0.721
B3	0.141	0.465	0.668	0.128	0.471	0.668	0.529	0.516	0.888
B4	0.417	0.741	0.835	0.435	0.760	0.835	0.917	0.950	0.554
B5	0.234	0.234	0.724	0.224	0.232	0.722	0.675	0.150	0.865
B6	0.510	0.510	0.891	0.531	0.521	0.888	0.062	0.583	0.532
B7	0.955	0.955	0.556	0.918	0.942	0.555	0.369	0.861	0.698
B8	0.659	0.152	0.866	0.675	0.157	0.865	0.833	0.806	0.947
B9	0.103	0.596	0.533	0.062	0.577	0.532	0.217	0.228	0.614
B10	0.383	0.875	0.700	0.369	0.867	0.699	0.527	0.517	0.781
B11	0.791	0.791	0.946	0.831	0.815	0.948	0.985	0.445	0.968
B12	0.238	0.238	0.614	0.219	0.235	0.615	0.372	0.865	0.634
B13	0.514	0.514	0.781	0.525	0.525	0.781	0.679	0.155	0.801
B14	0.948	0.436	0.967	0.988	0.453	0.967	0.445	0.134	0.667
B15	0.393	0.882	0.634	0.373	0.873	0.634	0.752	0.424	0.834
B16	0.670	0.158	0.800	0.681	0.162	0.800	0.060	0.714	0.000
B17	0.465	0.141	0.668	0.449	0.138	0.667	0.141	0.853	0.500
B18	0.741	0.417	0.835	0.756	0.427	0.834	0.081	0.064	0.917
B19	0.021	0.698	0.999	0.064	0.719	0.000	0.466	0.482	0.584
B20	0.183	0.860	0.500	0.141	0.846	0.500	0.775	0.775	0.750
B21	0.042	0.042	0.915	0.075	0.053	0.916	0.788	0.111	0.666
B22	0.491	0.491	0.583	0.464	0.473	0.583	0.096	0.400	0.833
B23	0.767	0.767	0.749	0.770	0.763	0.750	0.484	0.830	0.500
B24	0.805	0.125	0.665	0.793	0.114	0.666	0.171	0.665	0.866
B25	0.081	0.402	0.831	0.099	0.403	0.833	0.559	0.099	0.533
B26	0.523	0.846	0.499	0.484	0.822	0.500	0.864	0.376	0.700
B27	0.152	0.659	0.866	0.173	0.671	0.866	0.326	0.302	0.886
B28	0.596	0.103	0.533	0.560	0.092	0.532	0.714	0.737	0.553
B29	0.875	0.383	0.700	0.866	0.382	0.699	0.020	0.013	0.719
B30	0.305	0.305	0.886	0.324	0.311	0.886	0.482	0.961	0.968
B31	0.750	0.750	0.553	0.711	0.731	0.553	0.868	0.381	0.635
B32	0.029	0.029	0.719	0.018	0.021	0.719	0.176	0.670	0.802

B33	0.436	0.948	0.967	0.482	0.967	0.968	0.014	0.016	0.612
B34	0.882	0.393	0.634	0.869	0.387	0.635	0.321	0.306	0.779
B35	0.158	0.670	0.800	0.176	0.677	0.801	0.627	0.596	0.946
B36	0.402	0.081	0.831	0.015	0.021	0.612	0.127	0.478	0.332
B37	0.846	0.523	0.499	0.322	0.310	0.779	0.433	0.767	0.166
B38	0.125	0.805	0.665	0.629	0.600	0.946	0.223	0.238	0.279
B39	0.142	0.463	0.331	0.128	0.471	0.332	0.530	0.528	0.112
B40	0.419	0.739	0.165	0.435	0.760	0.166	0.917	0.948	0.446
B41	0.662	0.151	0.134	0.224	0.232	0.279	0.676	0.163	0.135
B42	0.108	0.596	0.467	0.531	0.521	0.112	0.062	0.583	0.468
B43	0.386	0.874	0.300	0.918	0.942	0.446	0.368	0.874	0.302
B44	0.794	0.794	0.053	0.675	0.157	0.135	0.830	0.807	0.053
B45	0.239	0.239	0.386	0.062	0.577	0.468	0.218	0.242	0.386
B46	0.515	0.515	0.219	0.369	0.867	0.302	0.524	0.531	0.219
B47	0.948	0.441	0.033	0.831	0.815	0.053	0.985	0.445	0.033
B48	0.392	0.885	0.366	0.219	0.235	0.386	0.373	0.879	0.366
B49	0.669	0.161	0.200	0.525	0.525	0.219	0.680	0.168	0.200
B50	0.463	0.142	0.331	0.988	0.453	0.033	0.448	0.144	0.333
B51	0.739	0.419	0.165	0.373	0.873	0.366	0.755	0.433	0.166
B52	0.053	0.053	0.083	0.681	0.162	0.200	0.078	0.062	0.084
B53	0.502	0.502	0.415	0.449	0.138	0.333	0.463	0.480	0.417
B54	0.777	0.777	0.249	0.756	0.427	0.166	0.769	0.769	0.250
B55	0.803	0.127	0.335	0.075	0.053	0.084	0.792	0.120	0.334
B56	0.079	0.403	0.168	0.464	0.473	0.417	0.099	0.410	0.167
B57	0.361	0.684	0.000	0.770	0.763	0.250	0.403	0.691	0.000
B58	0.151	0.662	0.134	0.793	0.114	0.334	0.172	0.679	0.134
B59	0.596	0.108	0.467	0.099	0.403	0.167	0.559	0.099	0.468
B60	0.874	0.386	0.300	0.407	0.695	0.000	0.865	0.389	0.301
B61	0.306	0.306	0.114	0.173	0.671	0.134	0.327	0.316	0.114
B62	0.753	0.753	0.446	0.560	0.092	0.468	0.711	0.738	0.447
B63	0.030	0.030	0.281	0.866	0.382	0.301	0.017	0.027	0.281
B64	0.441	0.948	0.033	0.324	0.311	0.114	0.482	0.961	0.032
B65	0.885	0.392	0.366	0.711	0.731	0.447	0.869	0.394	0.365
B66	0.161	0.669	0.200	0.018	0.021	0.281	0.175	0.683	0.198
B67	0.034	0.034	0.391	0.482	0.967	0.032	0.015	0.028	0.388
B68	0.310	0.310	0.224	0.869	0.387	0.365	0.322	0.316	0.221
B69	0.589	0.589	0.056	0.176	0.677	0.199	0.627	0.594	0.054
B70	0.403	0.079	0.168	0.015	0.021	0.388	0.417	0.066	0.832
B71	0.684	0.361	0.000	0.322	0.310	0.221	0.111	0.777	0.666
B72	0.127	0.803	0.335	0.629	0.600	0.054	0.723	0.359	0.000

C1	0.040	0.040	0.613	0.419	0.095	0.833	0.739	0.024	0.000
C2	0.316	0.316	0.780	0.804	0.514	0.500	0.125	0.443	0.668
C3	0.593	0.593	0.948	0.112	0.806	0.666	0.432	0.732	0.834
C4	0.228	0.228	0.280	0.419	0.095	0.168	0.805	0.520	0.500
C5	0.504	0.504	0.113	0.727	0.387	0.000	0.419	0.101	0.168
C6	0.951	0.951	0.448	0.112	0.806	0.334	0.112	0.812	0.334
C7	0.888	0.888	0.896	0.913	0.909	0.895	0.923	0.912	0.897
C8	0.338	0.338	0.564	0.301	0.330	0.562	0.300	0.338	0.563
C9	0.612	0.612	0.731	0.606	0.620	0.729	0.616	0.624	0.730
C10	0.196	0.196	0.935	0.234	0.204	0.937	0.244	0.208	0.938
C11	0.644	0.644	0.602	0.622	0.625	0.604	0.632	0.627	0.604
C12	0.921	0.921	0.768	0.929	0.914	0.770	0.939	0.918	0.771
C13	0.900	0.900	0.102	0.913	0.909	0.105	0.912	0.917	0.104
C14	0.348	0.348	0.435	0.301	0.330	0.438	0.300	0.336	0.438
C15	0.623	0.623	0.268	0.606	0.620	0.271	0.605	0.626	0.271
C16	0.206	0.206	0.064	0.234	0.204	0.064	0.244	0.206	0.063
C17	0.656	0.656	0.396	0.622	0.625	0.397	0.621	0.632	0.397
C18	0.932	0.932	0.231	0.929	0.914	0.230	0.928	0.920	0.230

TABLE S4. The bond lengths (Å) in the icosahedral cages of the single crystal and 1-layer thick twinned B_4C.

	Single crystal		Twin A_1		Twin S_1 (layer A)		Twin S_1 (layer B)		Twin R_1	
	Left side	Right side	Left side	Right side	Left side	Right side	Left side	Right side	Left side	Right side
1	1.740	1.773	1.770	1.796	1.735	1.735	1.752	1.752	1.728	1.728
2	1.781	1.777	1.770	1.796	1.713	1.713	1.741	1.741	1.713	1.713
3	1.742	1.732	1.719	1.833	1.778	1.778	1.788	1.788	1.781	1.781
4	1.740	1.777	1.737	1.833	1.742	1.742	1.783	1.783	1.735	1.735
5	1.715	1.772	1.737	1.762	1.772	1.772	1.773	1.773	1.767	1.767
6	1.742	1.790	1.789	1.762	1.736	1.736	1.776	1.776	1.739	1.739
7	1.742	1.791	1.789	1.787	1.768	1.768	1.740	1.740	1.768	1.768
8	1.770	1.732	1.750	1.787	1.771	1.771	1.778	1.778	1.772	1.772
9	1.781	1.784	1.750	1.768	1.778	1.778	1.764	1.764	1.777	1.777
10	1.742	1.810	1.758	1.768	1.788	1.788	1.788	1.788	1.798	1.798
11	1.774	1.791	1.758	1.739	1.805	1.805	1.737	1.737	1.785	1.785
12	1.774	1.790	1.759	1.739	1.822	1.822	1.787	1.787	1.809	1.809
13	1.770	1.810	1.759	1.787	1.799	1.799	1.774	1.774	1.803	1.803
mean	**1.755**	**1.779**	**1.757**	**1.781**	**1.770**	**1.770**	**1.768**	**1.768**	**1.767**	**1.767**

TABLE S5. Calculated lattice constants and atomic coordinates for the 1-layer-thick twinned B_6N, $B_{13}CN$, and B_6O.

	B$_6$N			B$_{13}$CN			B$_6$O		
Parameter (Å, °)	$a =$ 5.077	$b =$ 5.379	$c =$ 8.680	$a =$ 5.140	$b =$ 5.140	$c =$ 8.874	$a =$ 5.151	$b =$ 5.386	$c =$ 8.761
	$\alpha =$ 90.000	$\beta =$ 90.000	$\gamma =$ 121.998	$\alpha =$ 90.000	$\beta =$ 90.000	$\gamma =$ 64.795	$\alpha =$ 90.000	$\beta =$ 90.000	$\gamma =$ 121.523
Atoms	x	y	z	x	y	z	x	y	z
B1	0.726	0.029	0.499	0.174	0.686	0.900	0.733	0.039	0.500
B2	0.337	0.336	0.999	0.325	0.325	0.835	0.357	0.351	0.998
B3	0.599	0.800	0.667	0.026	0.026	0.656	0.604	0.802	0.672
B4	0.395	0.432	0.601	0.686	0.174	0.900	0.384	0.430	0.598
B5	0.205	0.103	0.834	0.232	0.232	0.664	0.204	0.102	0.836
B6	0.995	0.731	0.896	0.528	0.528	0.839	0.006	0.742	0.897
B7	0.337	0.001	0.999	0.381	0.872	0.595	0.357	0.006	0.998
B8	0.726	0.697	0.499	0.872	0.381	0.595	0.733	0.694	0.500
B9	0.664	0.997	0.999	0.774	0.774	0.746	0.657	0.001	0.996
B10	0.053	0.694	0.499	0.423	0.101	1.000	0.033	0.689	0.498
B11	0.395	0.964	0.601	0.123	0.796	0.496	0.384	0.953	0.598
B12	0.185	0.592	0.663	0.178	0.687	0.095	0.186	0.593	0.660
B13	0.995	0.263	0.896	0.327	0.327	0.164	0.006	0.265	0.897
B14	0.791	0.895	0.831	0.031	0.031	0.339	0.786	0.893	0.824
B15	0.053	0.359	0.499	0.796	0.123	0.496	0.033	0.344	0.498
B16	0.664	0.666	0.999	0.101	0.423	1.000	0.657	0.656	0.996
B17	0.599	0.800	0.331	0.687	0.178	0.095	0.604	0.802	0.326
B18	0.395	0.432	0.396	0.235	0.235	0.335	0.384	0.430	0.400
B19	0.205	0.103	0.163	0.533	0.533	0.156	0.204	0.102	0.162
B20	0.995	0.731	0.101	0.136	0.458	0.500	0.006	0.742	0.100
B21	0.395	0.964	0.396	0.436	0.763	0.996	0.384	0.953	0.400
B22	0.185	0.592	0.334	0.385	0.874	0.400	0.186	0.593	0.338
B23	0.995	0.263	0.101	0.458	0.136	0.500	0.006	0.265	0.100
B24	0.791	0.895	0.167	0.763	0.436	0.996	0.786	0.893	0.174
B25	—	—	—	0.874	0.385	0.400	—	—	—
B26	—	—	—	0.785	0.785	0.246	—	—	—
C1	—	—	—	0.926	0.926	0.806	—	—	—
C2	—	—	—	0.633	0.633	0.306	—	—	—
N1	0.369	0.184	0.686	0.626	0.626	0.688	—	—	—
N2	0.021	0.511	0.811	0.934	0.934	0.188	—	—	—

N3	0.369	0.184	0.311	—	—	—	—	—	—
N4	0.021	0.511	0.186	—	—	—	—	—	—
O1	—	—	—	—	—	—	0.369	0.184	0.686
O2	—	—	—	—	—	—	0.021	0.511	0.810
O3	—	—	—	—	—	—	0.369	0.184	0.312
O4	—	—	—	—	—	—	0.021	0.511	0.188

Reference

[1] K.Y. Xie, K. Kuwelkar, R.A. Haber, J.C. LaSalvia, K.J. Hemker, Microstructural Characterization of a Commercial Hot-Pressed Boron Carbide Armor Plate, J. Am. Ceram. Soc. 99 (2016) 2834-2841.

[2] M.F. Toksoy, W. Rafaniello, K.Y. Xie, L. Ma, K.J. Hemker, R.A. Haber, Densification and characterization of rapid carbothermal synthesized boron carbide, Int. J. Appl. Ceram. Technol. 14 (2017) 443-453.

[3] U. Anselmi-Tamburiniw, Z.A. Munir, Y. Kodera, T. Imai, M. Ohyanagi, Influence of synthesis temperature on the defect structure of boron carbide: experimental and modeling studies, J. Am. Ceram. Soc. 88 (2005) 1382-1387.

[4] B. Chang, B.L. Gersten, S.T. Szewczyk, J.W. Adams, Characterization of boron carbide nanoparticles prepared by a solid state thermal reaction, Appl. Phys. A 86 (2007) 83-87.

[5] K.Y. Xie, Q. An, M.F. Toksoy, R.A. Haber, W.A. Goddard III, K.J. Hember, Atomic-Level Understanding of "Asymmetric Twins" in Boron Carbide, Phys. Rev. Lett. 115 (2015) 175501.

[6] P.H. Li, M.D. Ma, Y.J. Wu, X. Zhang, Y.K. Chang, Z.W. Zhuge, L. Sun, W.T. Hu, D. Yu, B. Xu, Z.S. Zhao, J.Y. Chen, J.L. He, Y.J. Tian, Preparation of dense B_4C ceramics by spark plasma sintering of high-purity nanoparticles, J. Eur. Ceram. Soc. 41 (2021) 3929-3936.

[7] P.H. Li, Y.Q. Bu, L.Y. Wang, C. Wang, J.Q. Huang, K. Tong, Y.J. Chen, J.L. He, Z.S. Zhao, B. Xu, Z.Y. Liu, G.Y. Gao, A.M. Nie, H.T. Wang, Y.J. Tian, In Situ Observation of Fracture along Twin Boundaries in Boron Carbide, Adv. Mater. 2204375 (2022) 1-7.